Modeling of strained quantum wires using eight-band k·p theory

O. Stier and D. Bimberg
Institut für Festkörperphysik, Technische Universität Berlin, Hardenbergstraβe 36, D-10623 Berlin, Germany
(Received 28 August 1996; revised manuscript received 30 October 1996)

We have calculated numerically the one-dimensional band structure and densities of states of a V-shaped $In_{0.2}Ga_{0.8}As/Al_xGa_{1-x}As$ single quantum wire using eight-band $\mathbf{k}\cdot\mathbf{p}$ theory. A finite-difference scheme is used for the calculations. The model includes the realistic orientation, shape, material composition, strain distribution, and piezoelectric charging of the wire. We find a dominant impact of the piezoelectric potential on the band structure and a marked spin splitting of the valence bands. Also, the conduction band is strongly nonparabolic. We propose an efficient procedure to calculate interior eigenvectors from Hamiltonians including conduction-band–valence-band interactions. This algorithm is 20–90 times faster than the best prevailing method and also applies to other Hamiltonians for the modeling of nanostructures, including those occurring in tight-binding or pseudopotential theory. [S0163-1829(97)04312-9]

I. INTRODUCTION

In recent years semiconductor quantum wires (QW's) have attracted growing interest for laser applications, mainly because of their potential for a reduction of the threshold current density[1,2] and their increased gain and differential gain achieved by multidimensional confinement.[3] A further enhancement of the gain and bandwidth of QW lasers is expected from the incorporation of strain.[4] Technological progress in the epitaxial fabrication of lattice-mismatched single and multiple QW's on nonplanar substrates led to various types of pseudomorphic QW's among which V-groove QW's have been intensively studied.

Parallel to the effort concerning the fabrication and characterization of strained QW's, their theoretical modeling was developed with increasing level of sophistication, in order to enable the prediction of the physical properties of such structures and to enable a deeper understanding of experimental results. *Unstrained* QW's of different shapes were investigated using the tight-binding[5] and effective bond-orbital[6] models as well as all the classical envelope function schemes: the parabolic band approximation (PBA),[7–9] the four-band Luttinger model,[10] the six-band Luttinger model,[11] and the eight-band $\mathbf{k}\cdot\mathbf{p}$ model.[12,13] On the other hand, *strained* QW's were studied only in the PBA (Refs. 14 and 15) and in the four-band[16] and six-band Luttinger models.[17] The main effort in these studies focused on a detailed treatment of the particular geometry. The interaction between the conduction bands (CB's) and valence bands (VB's) as included in many of the investigations of unstrained structures, however, has not been considered so far, although the indications for major modification of the CB (Refs. 18 and 19) also apply to the strained case.

In this paper we describe the modeling of a pseudomorphic V-groove QW by means of the eight-band $\mathbf{k}\cdot\mathbf{p}$ scheme in order to unify the CB-VB interaction and VB mixing with a detailed consideration of one of the most important realizations of one-dimensional (1D) structures. Our simulation accounts for the true geometrical shape of the wire and the graded barrier, the particular strain distribution, and the resulting piezoelectric charging of the structure. The impact of the strain on the band structure is visualized. A crucial part of our method is an efficient numerical procedure to generally calculate bound states in nanostructures under inclusion of the CB-VB interaction.

Our paper is organized as follows. In Sec. II we describe the QW sample, the approach used to describe the band structure by means of the eight-band $\mathbf{k}\cdot\mathbf{p}$ scheme, and the finite-difference method used for discretization. Section II A contains some necessary details about our assumptions regarding the strain, boundary conditions of envelope functions, and material parameters. Section II B presents the discretization of the Hamiltonian. In Sec. III we introduce a special algorithm for eigenvector extraction; its implementation is outlined in the Appendix. Section IV contains the results of our band-structure calculation and their discussion. In Sec. V we present a performance comparison between our algorithm and prevailing state-of-the-art methods, evidencing a one to two orders of magnitude acceleration of the calculation by our method.

II. BAND-STRUCTURE MODEL OF THE QW

The nanostructure we consider is a single V-groove QW (Ref. 20) with the nominal composition $In_{0.2}Ga_{0.8}As$ surrounded by a barrier of $Al_cGa_{1-c}As$, as shown in Fig. 1. The growth direction is [001]; we assign to it the geometrical coordinate y. The Al content c in the barrier increases linearly with the distance from the heterointerface in the y direction ($c=0.2$–0.7 within $\Delta y=200$ nm around the QW), thus the barrier forms a graded index separate confinement heterostructure (GRINSCH). The orientation of the QW is along $[1\bar{1}0]$, to which we assign the coordinate z. Then x refers to [110].

The lattice mismatch of $+1.4\%$ leads to mainly compressive strain in the QW. The particular strain distribution was calculated by a finite-element simulation for cubic materials, yielding the strain tensor $\hat{\epsilon}$ with respect to the crystal main axes as a function of the position in the QW cross-section plane (x,y).[14] From $\hat{\epsilon}(x,y)$ the piezoelectric polarization and its associated Coulomb potential $V_p(x,y)$ were calculated

$$V_p(\mathbf{r}) = -\frac{1}{4\pi\epsilon_0\epsilon_s}\int_{-\infty}^{\infty}\int_{-\infty}^{\infty}\int_{-\infty}^{\infty}\frac{\mathrm{div}[e_{14}(\mathbf{r}')\cdot\{\epsilon_{yz}+\epsilon_{zy},\epsilon_{xz}+\epsilon_{zx},\epsilon_{xy}+\epsilon_{yx}\}(\mathbf{r}')]}{|\mathbf{r}'-\mathbf{r}|}d\mathbf{r}'^3$$

(Ref. 14), where e_{14} is the piezoelectric module of the respective material at $\mathbf{r}'$ and ϵ_s is the static dielectricity constant. ϵ_s is taken to be constant all along the structure so that image charges need not be considered. Note that $V_p(\mathbf{r})$ possesses the same translation symmetry as the QW so that it is independent of z.

A. Eight-band k·p scheme for QW's

To calculate the 1D band structure in the direction z, where carrier transport is still possible, we used the eight-band $\mathbf{k}\cdot\mathbf{p}$ scheme as outlined previously for bulk materials[21] and quantum wells.[22] The model neglects strain gradient terms $\nabla\hat{\epsilon}(\mathbf{r})$ (Ref. 23) and the strain dependence of the spin-orbit interaction.[24] The static scalar potential $V_p(\mathbf{r})$ yields an additional diagonal contribution to the Hamiltonian that is not included in Refs. 21 and 22. Applied to a heterostructure, the $\mathbf{k}\cdot\mathbf{p}$ Hamiltonian $\hat{H}$ contains 21 spatially varying parameters, six of which appear in products with components of $\mathbf{k}$ so that $\hat{H}$ is originally not Hermitian. Therefore such products are symmetrized[12] according to

$$Qk_i \to (Qk_i + k_iQ)/2, \quad Qk_ik_j \to (k_iQk_j + k_jQk_i)/2 \qquad (i,j = x,y,z). \quad (1)$$

Under the assumption of identical zone-center Bloch functions in all materials, this implies the probability flux conservation at heterointerfaces.

To take advantage of the translational symmetry of the QW in $[110]$ we introduce wave-vector components k_x, k_y, k_z with respect to our geometrical coordinates.[11,16,22] Then the envelope functions are separable into a plane wave with the wave number k_z and an orthogonal part in the cross section plane (x,y). In this plane we use the spatial representation of $\hat{H}$ because then the material and strain distributions are most easy to handle. As a consequence, $k_x \mapsto -i\partial_x$ and $k_y \mapsto -i\partial_y$, while k_z remains a real number. We obtain a system

$$\hat{H}(x,y,k_z,\partial_x,\partial_y,\partial_{xx},\partial_{xy},\partial_{yy})\Psi(x,y) = E\Psi(x,y) \quad (2)$$

of eight partial differential equations for the eight complex envelope functions $\Psi = (\psi_{s\uparrow},\psi_{x\uparrow},\psi_{y\uparrow},\psi_{z\uparrow},\psi_{s\downarrow},\psi_{x\downarrow},\psi_{y\downarrow},\psi_{z\downarrow})$. The system depends continuously on k_z and its eigensolutions (E_n,Ψ_n) are the bound states of charge carriers in an arbitrarily oriented QW of arbitrary cross section, material composition, and strain distribution, including VB mixing and the CB-VB interaction. The well-known, general drawbacks[25] of the envelope-function approach are not expected to affect our results significantly since the QW is rather large and its band structure is calculated very close to the Γ point only, thus matching the validity conditions of the approach well.

Table I displays the material parameters we have used. From them, the missing parameters $P, A', L', M, N', l, m, n$ can be calculated at each position (x,y) according to Ref. 22. It is necessary that always $\gamma_1 \geqslant 1/m_{so}$ and that $A' > 0$, $L' < 0$, $M < 0$, and $N' < 0$. An important role for the carrier confinement play the band discontinuities at the heterointerfaces. We use composition-dependent E_v',[26] which we obtained from an overall fit to carefully selected data about heterojunctions involving AlGaAs, InGaAs, and InP from the reviews quoted in Table I. The deformation potentials were obtained from similar fits. B and b' are related to the polar nature of the materials and account for the microscopic lack of inversion symmetry, which causes spin splitting. However, in the presence of compressive strain this *micro*scopic effect is significantly smaller than that due to the *meso*scopic spatial asymmetry of the structure,[27] so that we set $B, b' = 0$.

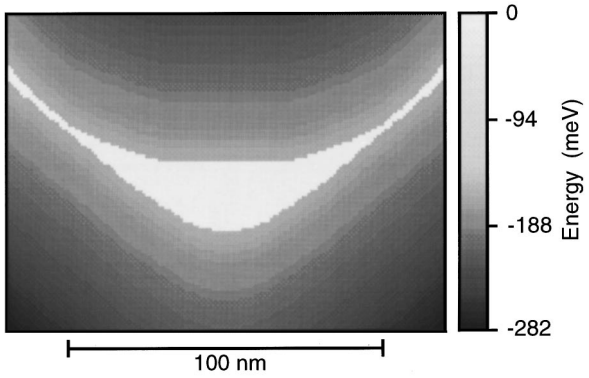

FIG. 1. The unstrained bulk valence band $E_v(x,y)$ in the heterostructure shows the GRINSCH structure of the barrier and the shape of the quantum-wire cross section (white). The pixel size is 1 nm^2, which is the true resolution in our calculations.

B. Finite-differences discretization

To obtain a matrix representation H of $\hat{H}$ we use a finite-difference method on a rectangular grid with square unit cells and $\tilde{N} = N_xN_y$ nodes. The real and imaginary parts of the envelopes ψ are represented by $\tilde{N}$-dimensional vectors each. Accordingly, the differential operators and spatially varying parameters in Eq. (2) become $\tilde{N}\times\tilde{N}$ real matrices, H is an $8\tilde{N}\times 8\tilde{N}$ complex matrix, and the final dimension of Ψ is $N = 16\tilde{N}$. The parameter matrices are diagonal. The matrices for the derivatives must be chosen carefully to reproduce the symmetry properties and the commutation relations of the $\mathbf{k}$ components and to ensure numerical stability of the difference scheme.

To accomplish this we introduce two different matrices $D^{(+)}$ and $D^{(-)}$ for both ∂_x and ∂_y with $[D^{(+)}]^T = -D^{(-)}$. The $D^{(+)}$ are used in the upper right half of H and the $D^{(-)}$ in the lower left half only. The discretizations of the symmetrized expressions for $Q\partial_x, Q\partial_y, Q\partial_{xx}, Q\partial_{xy}, Q\partial_{yy}$

TABLE I. Input material parameters for 300 K used in the calculations. The asterisk denotes a second-order Chebyshev approximation to $1424+1594c+c(c-1)(1310c-127)$ for $c \leqslant 0.45$.

Quantity	in $In_cGa_{1-c}As$	Reference	in $Al_cGa_{1-c}As$	Reference
E_0 (meV)	$1424-1501c+433c^2$	28	$1428+1572c-553c^2$ (*)	29
E_v' (meV)	$-6920+231c-58c^2$	26,28	$-6920-433c-24c^2$	29,30
Δ_0 (meV)	$340-93c+133c^2$	31	$340-131c+71c^2$	29
m_e (m_0)	$0.0667-0.0419c$	32	$0.067+0.083c$	29
m_{so} (m_0)	$0.163-0.023c$	29,32	$0.165+0.135c$	29
γ_1	$1/[(1-c)/7.10+c/19.7]$	31,33	$1/[(1-c)/7.10+c/3.76]$	29
γ_2	$1/[(1-c)/2.02+c/8.4]$	31,33	$1/[(1-c)/2.02+c/0.90]$	29
γ_3	$1/[(1-c)/2.91+c/9.3]$	31,33	$1/[(1-c)/2.91+c/1.42]$	29
B (meV nm^2)	0	22,27	0	22,27
b' (meV)	0	22,27	0	22,27
a_c (meV)	$-8013+2933c$	32	$-8013+2373c$	26
a_g (meV)	$-8233+2153c$	32	$-8233+123c$	26
b_v (meV)	$-1824+24c$	31	$-1824+124c$	26
d_v (meV)	$-5062+1462c$	31	$-5062+512c$	26
C_{11} (GPa)	$118.8-35.5c$	31,33	$118.8+1.4c$	29
C_{12} (GPa)	$53.8-8.5c$	31,33	$53.8+3.2c$	29
C_{44} (GPa)	$59.4-19.8c$	31,33	$59.4-0.5c$	29
ϵ_s	$13.18+1.42c$	32	13.46	
e_{14} (C m^{-2})	$0.160-0.115c$	32	0.137	

are then obtained from the standard first-order forward (backward) difference quotients $\partial_x^{(+)}, \partial_y^{(+)} (\partial_x^{(-)}, \partial_y^{(-)})$ by

$$D_x^{(+)}(Q) = [Q\partial_x^{(+)} + \partial_x^{(+)} Q]/2,$$

$$D_x^{(-)}(Q) = [Q\partial_x^{(-)} + \partial_x^{(-)} Q]/2,$$

$$D_y^{(+)}(Q) = [Q\partial_y^{(+)} + \partial_y^{(+)} Q]/2,$$

$$D_y^{(-)}(Q) = [Q\partial_y^{(-)} + \partial_y^{(-)} Q]/2,$$

$$D_{xx}(Q) = [\partial_x^{(+)} Q \partial_x^{(-)} + \partial_x^{(-)} Q \partial_x^{(+)}]/2,$$

$$D_{yy}(Q) = [\partial_y^{(+)} Q \partial_y^{(-)} + \partial_y^{(-)} Q \partial_y^{(+)}]/2,$$

$$D_{xy}(Q) = [\partial_x^{(+)} Q \partial_y^{(+)} + \partial_y^{(+)} Q \partial_x^{(+)} + \partial_x^{(-)} Q \partial_y^{(-)} + \partial_y^{(-)} Q \partial_x^{(-)}]/4.$$

Expanding these matrix expressions gives the difference quotients we have used. For $Q = qI$ (where I is the identity matrix and $q \in \mathbb{R}$) all of them reduce to standard difference quotients. The handling of boundary nodes for the realization of Dirichlet and Neumann conditions is standard. H was implemented as a sequence of linear operations on single envelope vectors ψ. We used $N_x = 137$, $N_y = 99$, and $d = 1$ nm, so that $N = 217\,008$. One $H\Psi$ multiplication consists of 208 linear combinations, 304 parameter multiplications, and 104 partial differentiations of complex $\widetilde{N}$ vectors, amounting to 47 MegaFLOP in total.

III. EFFICIENT ALGORITHM FOR EIGENVECTOR CALCULATION

To solve Eq. (2) for eigenstates Ψ_n near the band edges we use an algorithm developed by ourselves that is a combination of the generalized Davidson algorithm[34,35] (GDA) with residual minimization (RM).[36] Although such a combination has been discussed earlier for the purpose of calculating *extreme* eigenvalues,[35,36] its principal advantage over prevailing methods for the calculation of *interior* eigenvalues, as required here, was never acknowledged.

The calculation of interior eigenvalues is an intricate problem if the matrix H cannot be stored, factorized, or inverted, which is the case here. The classical iterative eigensolution methods, i.e., subspace iteration, molecular dynamics simulation, Chebyshev iteration, conjugate gradients (CG), Lanczos algorithm (LA), and also the *usual* GDA by their mathematical nature yield only extreme eigenvalues; this cannot be altered by preconditioning. Hence interior eigenvalues are obtained by these algorithms only after a spectral transformation of H. As the preferable shift-and-invert operation $H \mapsto (H-\epsilon I)^{-1}$ is not available, the quadratic transform $H \mapsto (H-\epsilon I)^2$ can be used, where ϵ is the search energy specifying the closest eigenvalue E_n as the wanted one. The latter replacement is known as the folded spectrum method (FSM) and usually combined with the CG (Refs. 37 and 38) or variants of the LA.[39] Due to their well-known mathematical relationship the CG and LA exhibit no dramatic difference of their convergence properties, which elevates them to be the most powerful elegant basic algorithms. Regrettably, the FSM causes a severe decrease of the local convergence rate of all mentioned iterations, as can easily be derived from the spectral structures of H and $(H-\epsilon I)^2$. We now present a method avoiding this drawback.

Other than in the CG and LA, in the Davidson-type algorithms the (i) subspace construction and (ii) variational calculation of the eigenvector approximations are explicitly separated. The eigenvector to which the iteration converges is solely determined by (ii), while the convergence rate

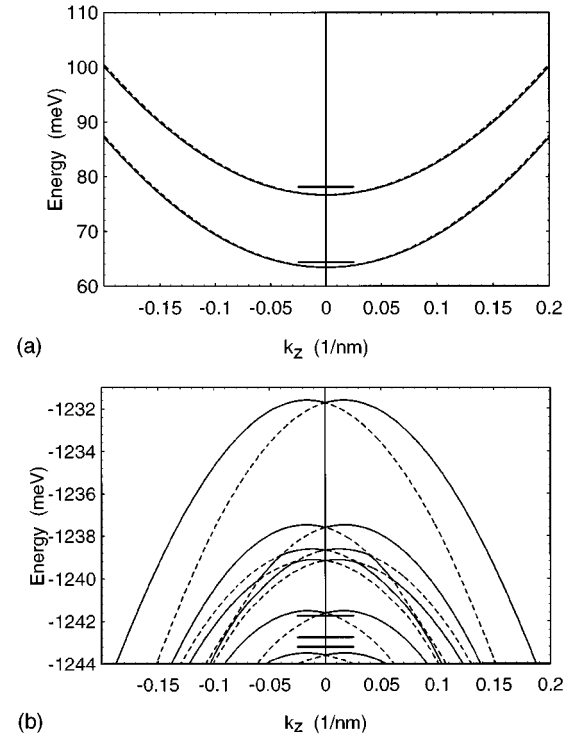

FIG. 2. Lowest four 1D conduction bands and topmost twelve 1D valence bands in the quantum wire (alternating solid and dashed). The energy zero is E_c of unstrained bulk $In_{0.2}Ga_{0.8}As$. The solid markers indicate the quantum levels calculated by a parabolic band approximation.

mainly depends on (i). This offers the unique opportunity to use H in (i) and $(H-\epsilon I)^2$ in (ii). The result is that convergence to interior eigenpairs occurs almost as fast as towards extreme ones. Since the Rayleigh-Ritz (Ritz-Galerkin) procedure commonly employed for (ii) applied to $(H-\epsilon I)^2$ is equivalent to the RM with respect to (H,ϵ), the method obtained is a RM GDA operating on H.

We show below that the RM GDA in fact is one to two orders of magnitude more efficient than the FSM and thus certainly the fastest algorithm for our purpose at present. Clearly, it can be applied to any other Hamiltonian accounting for the CB-VB interaction (as in tight-binding or pseudopotential methods) and to any other kind of nanostructure (e.g., quantum dots) as well. Hence the RM GDA appears to be a valuable general-purpose tool for the entire field of nanostructure band-structure research. Its implementation is described in the Appendix.

IV. DISCUSSION OF THE BAND STRUCTURE

Figure 2 shows the lowest four 1D conduction bands and the topmost twelve 1D valence bands in the z direction for k_z between $\pm 0.2\,\mathrm{nm}^{-1}$. All curves were calculated separately with individual ϵ, i.e., no block algorithm was used. For $k_z=0$ we started with a Gaussian random vector and for other k_z values the result of the previous one was taken as an initial guess and ϵ was adjusted by second-order extrapolation.

The zero energy is the minimum of E_c over the entire structure, i.e., the CB edge of unstrained bulk $In_{0.2}Ga_{0.8}As$.

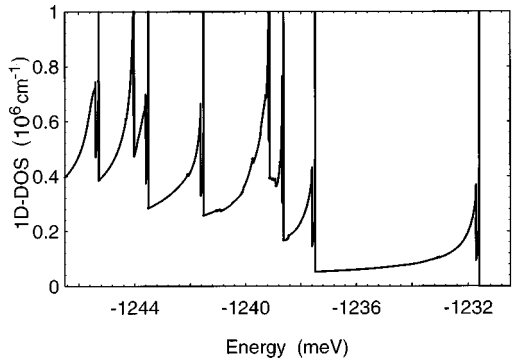

FIG. 3. Double peaks in the VB DOS reflect the spin splitting.

The VB states are labeled from top to bottom by $|1,1\rangle$, $|1,2\rangle$, $|2,1\rangle$, $|2,2\rangle$, . . . to account for the spin; the $|,1\rangle$ states belong to solid lines and the $|,2\rangle$ states to dashed lines. As can be seen, there is no band crossing except for $k_z=0$.[40]

Between the $|,1\rangle$ and $|,2\rangle$ states we observe a meV range splitting for $k_z\neq 0$. This spin splitting is caused by the mesoscopic violation of the spatial inversion symmetry, which is due to the irregular geometrical shape of the QW, strain field, and piezoelectric charging. The spin splitting leads to bimodal peaks in the density of states (DOS) consisting of a true singularity accompanied by a finite discontinuity. This is seen in the VB DOS; see Fig. 3. In general, the spin splitting will cause slightly increased linewidths of all transitions, as compared to the unsplit case, and presents a lower limit of the linewidth for disappearing interface roughness. Figure 4 shows the resulting joint DOS for **k**-conserving transitions and visualizes clearly the dominance of the true singularities at all subband edges. It is well known that the existence of such singularities largely improves the performance of semiconductor lasers.[41]

The Coulomb potential V_p stemming from the piezoelectric interface charging is repulsive for holes and thus effectively reduces the actually tapered QW thickness from <23 nm to uniformly ≈ 7 nm. Hence, for holes the QW looks approximately like a bent quantum well. This practically leads to the formation of three coupled sub-QW's along the lower interface, which have separate ground states at $k_z=0$; see Fig. 5. The lowest of these, the true ground state

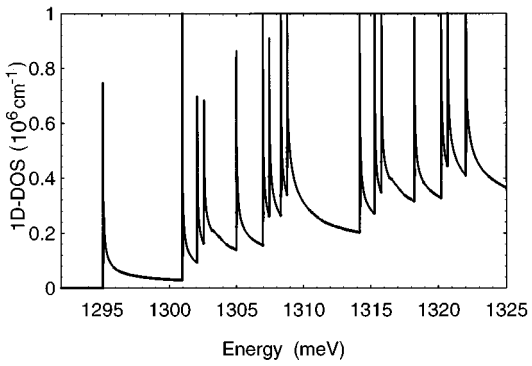

FIG. 4. Joint DOS for **k**-conserving transitions (without broadening). The dipole matrix elements $|\langle a|\hat{\mathbf{e}}\cdot\vec{\mathbf{p}}|b\rangle|^2$ between $\langle a|$ and spin split states $|b,1\rangle$, $|b,2\rangle$ may differ by a factor 100, thus demonstrating the well-known spin-selection rule.

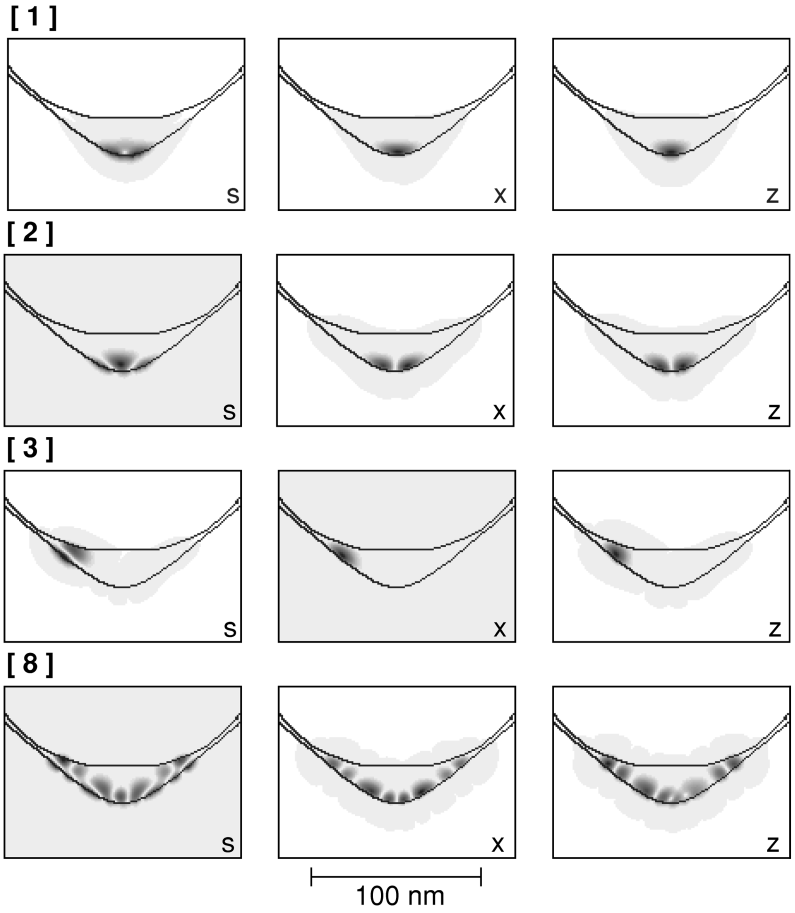

FIG. 5. Envelopes $|\psi|^2$ of the Bloch functions $|s\uparrow\rangle$, $|x\uparrow\rangle$, and $|z\uparrow\rangle$ in the VB states $|1,\rangle$, $|2,\rangle$, $|3,\rangle$, and $|8,\rangle$ at $k_z=0$.

$|1,\rangle$ is located in the center as usual and succeeded by its first excited state $|2,\rangle$. The next two states $|3,\rangle$ and $|4,\rangle$, have a quantization energy that is ≈ 7 meV larger , while their separation is only ≈ 0.5 meV. This gives rise to a weak left-right symmetry breaking producing the two other quasi-ground-states. Figure 5 shows the leftmost of them. Symmetry breaking in this QW was previously discussed by us in the PBA, which neglects any band mixing.[14] There the symmetry breaking was found to concern the true ground state $|1,\rangle$. Our present $\mathbf{k}\cdot\mathbf{p}$ calculation reveals this slight inaccuracy and indicates that parabolic band approximations are unsuited in such complex situations involving strain and piezoelectricity within an irregular geometry. The main source of inaccuracy of the PBA in the case of irregular geometry is that different states (here $|1,\rangle$ and $|3,\rangle$) may experience different directions of strongest confinement. The effective masses are not flexible enough to resemble this situation in the Hamiltonian. For a direct comparison with a PBA calculation using the heavy hole masses $m([110])$ in the x and $m([001])$ in the y direction see the solid markers in Fig. 2.

In addition, the CB is essentially nonparabolic: for $k_z=0-1.4$ nm^{-1} the ground-state relative effective mass rises from 0.066 to 0.208; see Fig. 6. Due to the large size of the QW the electron effective mass approximately takes on its bulk value at $k_z=0$ and the previously predicted[18] increase occurs at higher wave numbers only, when the wave function is more affected by the structural and piezoelectric confinement. This demonstrates the importance of including the CB-VB interaction in the modeling, otherwise no reasonable prediction of the CB dispersion is possible.

Fortunately, this is available at a comparable computational expense as for a separate treatment of the CB and VB or for a perturbational approximation of their interaction, namely, by means of the eigensolution algorithm presented in the Appendix. To prove the tremendous savings achieved by this method we finally report a comparison with the well-established FSM.

V. ASSESSMENT OF THE ALGORITHM

In regard to the eigenstate iteration, the spin splitting produces a more adverse spectral structure of H for $k_z=0.02$ nm^{-1} than for $k_z=0$ because the separations between distinct eigenvalues decrease. To compare the RM

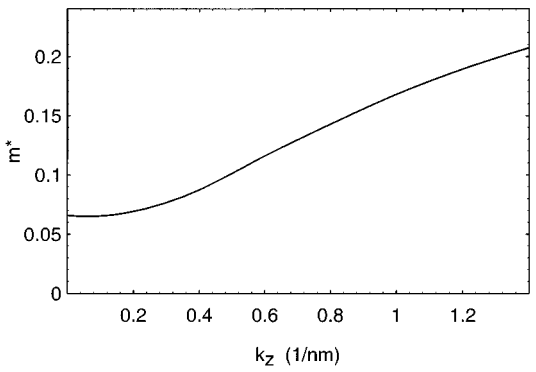

FIG. 6. Relative effective mass $[1\bar{1}0]$ in the $|1,1\rangle$ CB state. The nonparabolicity of the CB due to the $\mathbf{k}\cdot\mathbf{p}$ interaction is obvious.

TABLE II. Effective local convergence rates (CR's) for different spectral structures of H (due to different k_z) and restarting lengths $S_{\max}$. $\overline{\phi}$ is the *average* CR and $\phi_{\max}$ the *maximum* CR encountered in the local phase ($||\mathbf{r}||<0.5$ meV) of the respective run.

Method	$S_{\max}$	$k_z=0$ nm^{-1}	$k_z=0.02$ nm^{-1}
FSM	11	$\overline{\phi}=0.0008$	$\overline{\phi}=0.0001$
		$\phi_{\max}=0.0008$	$\phi_{\max}=0.0007$
	19	$\overline{\phi}=0.0009$	$\overline{\phi}=0.0003$
		$\phi_{\max}=0.0009$	$\phi_{\max}=0.0008$
RM GDA	11	$\overline{\phi}=0.0179$	$\overline{\phi}=0.0090$
		$\phi_{\max}=0.0179$	$\phi_{\max}=0.0215$
	19	$\overline{\phi}=0.0263$	$\overline{\phi}=0.0157$
		$\phi_{\max}=0.0263$	$\phi_{\max}=0.0297$

GDA with the FSM we have calculated the VB ground state $|1,1\rangle$ at both k_z values and with two different restarting lengths $S_{\max}$. The runs were started with Gaussian random vectors and $\epsilon=-1230$ meV. Table II comprises the effective local convergence rates ϕ observed in these eight runs. ϕ is defined as $\phi=-\log_{10}\kappa/z$, where κ is the local convergence factor of the residual norm and z is the number of $H\mathbf{x}$ multiplications per iteration cycle. Note that $z=1$ for the RM GDA, while $z=2$ for the FSM. Figure 7 shows the residual norm versus the $H\mathbf{x}$ multiplication count for $k_z=0.02$ nm^{-1} and $S_{\max}=19$.

We find the following in ample accordance with the theoretical analysis. (i) The RM GDA is a factor 22 – 90 faster than the FSM (measured by ϕ). (ii) The more complicated spectrum of H for $k_z=0.02$ nm^{-1} leads to slower and nonmonotonic local convergence of both methods. For $k_z=0$ the local convergence is uniform so that $\phi=\phi_{\max}$. In contrast, the global convergence is hardly affected. (iii) Restarting earlier slows down the local convergence. Therefore, we used $S_{\max}\approx 30$ in all other runs. We conclude that the RM GDA is by far the fastest algorithm to calculate interior eigenpairs of at least the $\mathbf{k}\cdot\mathbf{p}$ Hamiltonian operators.

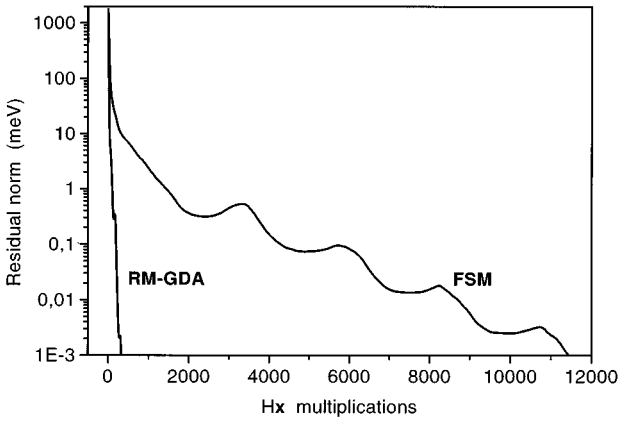

FIG. 7. Typical convergence behavior of the RM GDA and the well-known FSM. The onset of the local convergence at $||\mathbf{r}||\approx 1$ meV is shown clearly. Restarting was performed at a length of $S_{\max}=19$ vectors.

VI. SUMMARY

We have calculated the one-dimensional band structure of a realistic, pseudomorphic $In_{0.2}Ga_{0.8}As/Al_xGa_{1-x}As$ V-groove quantum wire in eight-band $\mathbf{k}\cdot\mathbf{p}$ theory. The $\mathbf{k}\cdot\mathbf{p}$ Hamiltonian was discretized using a finite-difference method specially designed to realize flux conservative matching of the envelopes at the heterointerfaces. The cross-section shape of the wire was taken directly from a TEM image and digitalized with 1-nm resolution, giving 13 563 pixels. The calculation fully accounts for the graded barrier, the particular strain distribution, and the resulting piezoelectric charging of the structure. We found a dominant impact of the strain-induced piezoelectricity on the band structure and a marked spin splitting of the valence bands due to the mesoscopic lack of spatial inversion symmetry. The conduction band is strongly nonparabolic.

To calculate arbitrary eigenstates from discrete Hamiltonians that include both CB's and VB's we have developed a residual minimization variant of the generalized Davidson algorithm. This algorithm serves the same purpose as the folded spectrum method,[38,39] but in our case exhibits one or two orders of magnitude faster local convergence than the latter.

We like to emphasize that the algorithm can readily be applied to any other Hamiltonian describing single particles in nanostructures as well, e.g., in the frame of tight-binding or pseudopotential calculations. The computational progress established by this work is not restricted to the envelope-function approach.

ACKNOWLEDGMENTS

The authors would like to thank M. Grundmann for having calculated the strain and piezoelectric charging of the QWR and for many helpful discussions. Sincere gratitude is also due to P. Enders and D. Suisky for valuable discussion about $\mathbf{k}\cdot\mathbf{p}$ theory. This work was funded by Deutsche Forschungsgemeinschaft in the framework of SFB 296.

APPENDIX: IMPLEMENTATION OF THE RM GDA

We describe the calculation of one eigenvector only; the simultaneous operation is straightforward. One iteration cycle consists of the following steps.

(i) The orthonormal trial vectors $\mathbf{x}^{(s)}$ from the steps $s=1,\ldots,S$ and their images $\mathbf{y}^{(s)}=(H-\epsilon I)\mathbf{x}^{(s)}$ are stored on disk. The $S\times S$ RM projection matrix $P^{(S)}=(p_{ij})$ with

$$p_{ij}=\langle\mathbf{x}^{(i)}|(H-\epsilon I)^2\mathbf{x}^{(j)}\rangle=\langle\mathbf{y}^{(i)}|\mathbf{y}^{(j)}\rangle \tag{A1}$$

is in the core memory.

(ii) The variational eigenvector approximation $\mathbf{v}$ and its image $\mathbf{w}$ are calculated from the lowest, normalized eigenvector $\vec{u}=(u_1,\ldots,u_S)$ of $P^{(S)}$,

$$\mathbf{v}=\sum_{s=1}^{S}u_s\mathbf{x}^{(s)},\quad \mathbf{w}=\sum_{s=1}^{S}u_s\mathbf{y}^{(s)},$$

and stored on disk.

(iii) The Rayleigh quotient $\mu=\langle\mathbf{v}|\mathbf{w}\rangle$ and the residual $\mathbf{r}=\mathbf{w}-\mu\mathbf{v}$ are calculated.

(iv) If $||\mathbf{r}|| < \epsilon$ the procedure terminates, and $\Psi = \mathbf{v}$ and $E = \mu$ are returned.

(v) σ is chosen according to a shifting strategy and the preconditioner $C = M - \sigma I$ is prepared. In particular, $M = \mathrm{diag}(H)$ and $\sigma = \mu$ constitute the nongeneralized Davidson algorithm. The pseudoresidual $\mathbf{q} = C^{-1}\mathbf{r}$ is calculated and orthonormalized against $\mathbf{x}^{(1)}, \ldots, \mathbf{x}^{(S)}$, giving $\tilde{\mathbf{q}}$.

(vi) If the storage of $2S+4$ vectors would exceed the disk capacity the algorithm is restarted: all $\mathbf{x}^{(s)}$, all $\mathbf{y}^{(s)}$, and $P^{(S)}$ are disposed; $\mathbf{v}^{(S-1)}$ is orthonormalized against $\mathbf{v}^{(S)}$ and $\mathbf{w}^{(S-1)}$ is updated accordingly; $\mathbf{v}^{(S-1)}$, $\mathbf{w}^{(S-1)}$, $\mathbf{v}^{(S)}$, and $\mathbf{w}^{(S)}$ are stored on disk as $\mathbf{x}^{(1)}$, $\mathbf{y}^{(1)}$, $\mathbf{x}^{(2)}$, and $\mathbf{y}^{(2)}$, respectively; and $S \mapsto 2$ and $P^{(2)}$ is calculated from $\mathbf{y}^{(1)}$ and $\mathbf{y}^{(2)}$ according to Eq. (A1). Otherwise $\mathbf{v}^{(S-1)}$ and $\mathbf{w}^{(S-1)}$ are disposed from disk.

(vii) $\tilde{\mathbf{q}}$ is stored on disk as $\mathbf{x}^{(S+1)}$ and $S \mapsto S+1$.

(viii) The image of the new basis vector is calculated, $\mathbf{y}^{(S)} = (H - \epsilon I)\mathbf{x}^{(S)}$, and $P^{(S)}$ is updated by $\mathbf{y}^{(S)}$ according to Eq. (A1).

We note that $\tilde{\mathbf{q}}$ can be obtained from a different procedure from step (v) as well, for instance, by the one suggested in Ref. 42.

[1] M. Walther, E. Kapon, E. Colas, D. M. Hwang, and R. Bhat, Appl. Phys. Lett. **60**, 521 (1991).

[2] S. Tiwari, G. D. Pettit, K. R. Milkove, F. Legoues, R. J. Davis, and J. M. Woodall, Appl. Phys. Lett. **64**, 3536 (1994).

[3] M. Asada, Y. Miyamoto, and Y. Suematsu, IEEE J. Quantum Electron. **22**, 1915 (1986).

[4] E. Kapon, D. M. Hwang, M. Walther, R. Bhat, and N. G. Stoffel, Surf. Sci. **267**, 593 (1992).

[5] Y. Arakawa, Y. Yamauchi, and J. N. Schulman, Phys. Rev. B **43**, 4732 (1991).

[6] D. S. Citrin and Y. Chang, IEEE J. Quantum Electron. **29**, 97 (1993).

[7] T. Tadić and Z. Ikonić, Phys. Rev. B **50**, 7680 (1994).

[8] G. Bastard and J. Marzin, Solid State Commun. **91**, 39 (1994).

[9] R. Rinaldi, R. Cingolani, M. Lepore, M. Ferrara, I. M. Catalano, F. Rossi, L. Rota, E. Molinari, P. Lugli, U. Marti, D. Martin, F. Morier-Gemoud, P. Ruterana, and F. K. Reinhart, Phys. Rev. Lett. **73**, 2899 (1994).

[10] J. C. Yia and N. Dagli, IEEE J. Quantum Electron. **31** 208 (1995).

[11] M. Notomi, S. Nojima, M. Okamoto, H. Iwamura, T. Tamamura, J. Hammersberg, and H. Weman, Phys. Rev. B **52**, 11 073 (1995).

[12] G. A. Baraff and D. Gershoni, Phys. Rev. B **43**, 4011 (1991).

[13] L. Pfeiffer, H. Baranger, D. Gershoni, K. Smith, and W. Wegscheider, in *Low Dimensional Structures Prepared by Epitaxial Growth or Regrowth on Patterned Substrates*, edited by K. Eberl, P. M. Petroff, and P. Demeester, Vol. 298 of *NATO Advanced Study Institute, Series E: Applied Science* (Kluwer, Dordrecht, 1995), p. 93.

[14] M. Grundmann, O. Stier, and D. Bimberg, Phys. Rev. B **50**, 14 187 (1994).

[15] L. De Caro and L. Tapfer, J. Appl. Phys. **79**, 9188 (1996).

[16] I. Vurgaftman, J. M. Hinckley, and J. Singh, IEEE J. Quantum Electron. **30**, 75 (1994).

[17] M. Notomi, J. Hammersberg, H. Weman, S. Nojima, H. Sugiura, M. Okamoto, H. Iwamura, T. Tamamura, and M. Potemski, Phys. Rev. B **52**, 11 147 (1995).

[18] R. Chen and K. K. Bajaj, Phys. Rev. B **50**, 1949 (1994).

[19] A. T. Meney and G. Jones, Appl. Phys. Lett. **67**, 1512 (1995).

[20] M. Grundmann, V. Türck, J. Christen, E. Kapon, D. M. Hwang, C. Caneau, R. Bhat, and D. Bimberg, Solid State Electron. **37**, 1097 (1994).

[21] P. Enders, A. Bärwolff, M. Woerner, and D. Suisky, Phys. Rev. B **51**, 16 695 (1995).

[22] D. Gershoni, C. Henry, and G. Baraff, IEEE J. Quantum Electron. **29**, 2433 (1993).

[23] Y. Zhang, Phys. Rev. B **49**, 14 352 (1994).

[24] M.-E. Pistol, M. Gerling, D. Hessman, and L. Samuelson, Phys. Rev. B **45**, 3628 (1992).

[25] A. Zunger, in *Proceedings of the 23rd International Conference on the Physics of Semiconductors*, edited by M. Scheffler and R. Zimmermann (World Scientific, Singapore, 1996), p. 1341.

[26] C. G. Van de Walle, Phys. Rev. B **39**, 1871 (1989).

[27] O. Mauritz and U. Ekenberg, in *Proceedings of the 23rd International Conference on the Physics of Semiconductors* (Ref. 25), p. 1823.

[28] *Properties of Lattice-Matched and Strained Indium Gallium Arsenide*, edited by P. Bhattacharya (INSPEC, London, 1993).

[29] *Properties of Aluminium Gallium Arsenide*, edited by S. Adachi (INSPEC, London, 1993).

[30] E. T. Yu, J. O. McCaldin, and T. C. McGill, Solid State Phys. **46** 1 (1992).

[31] *Numerical Data and Functional Relationships in Science and Technology*, edited by O. Madelung, Landolt-Börnstein, New Series, Group III, Vol. 17, Pt. a (Springer, Berlin, 1982).

[32] S. Adachi, *Physical Properties of III-V Semiconductor Compounds* (Wiley, New York, 1992).

[33] *Properties of Gallium Arsenide*, 2nd ed. (INSPEC, London, 1990).

[34] E. R. Davidson, Comput. Phys. **7**, 519 (1993).

[35] C. W. Murray, S. C. Racine, and E. R. Davidson, J. Comp. Phys. **103**, 382 (1992).

[36] D. M. Wood and A. Zunger, J. Phys. A **18**, 1343 (1985).

[37] L. Wang and A. Zunger, in *Nanocrystalline Semiconductor Materials*, edited by P. V. Kamat and D. Meisel (Elsevier Science, New York, 1996).

[38] L. Wang and A. Zunger, J. Chem. Phys. **100**, 2394 (1994).

[39] G. Grosso, L. Martinelli, and G. P. Parravicini, Phys. Rev. B **51**, 13 033 (1995).

[40] O. Stier, M. Grundmann, and D. Bimberg, in *Proceedings of the 23rd International Conference on the Physics of Semiconductors* (Ref. 25), p. 1177.

[41] Y. Arakawa and H. Sakaki, Appl. Phys. Lett. **40**, 939 (1982).

[42] A. Booten and H. van der Vorst, Comp. Phys. **10**, 239 (1996).